



# Recent Advances on the Corrosion Resistance of Low-Density Steel: A Review

Chao Liu<sup>1,2</sup> · Yilun Li<sup>1,2</sup> · Xuequn Cheng<sup>1,2</sup> · Xiaogang Li<sup>1,2</sup>

Received: 26 August 2021 / Revised: 25 October 2021 / Accepted: 10 November 2021 / Published online: 15 February 2022  
© The Chinese Society for Metals (CSM) and Springer-Verlag GmbH Germany, part of Springer Nature 2022

## Abstract

This paper reviews the previous literature on the alloy composition design of low-density steel (LDS), focusing on the effect of Al, Mn, Ni, and other alloy elements on the formation of the steel matrix and second phase, and provides classification. The microstructure of LDS after processing includes the matrix structure,  $\kappa$ -carbide, and B2 (FeAl, NiAl, or MnAl) phase of ferritic LDS, austenitic LDS, and dual-phase LDS. The influence of alloy elements on the corrosion resistance of LDS is derived from the addition of Al and Mn for metallurgy. Additionally, the influence of Cr and Mo addition on the corrosion resistance improvement was studied. The electrochemical properties of the corrosion process in LDS are discussed. Further, the microstructure of LDS affects the corrosion resistance properties including pitting corrosion, hydrogen embrittlement, and SCC (stress corrosion cracking). Finally, future research directions are proposed.

**Keywords** Low-density steel · Alloy element adjustment · Microstructure · Corrosion resistance

## 1 Introduction

In the past decades, various types of low-density steels (LDSs) have been extensively designed to meet the increasing demands for steel strength, energy saving, and emission reduction that reduces the ecological burden in the automotive industry [1–5]. In the 1980s, Fe–Mn–Al–C LDS was considered as a substitute for austenitic Ni–Cr stainless steel because of its lower price. In terms of mechanical properties, Mn is used as an austenite stabilizer, and Al addition can significantly reduce the density of the material. Moreover, Al can also provide a passive film for the substrate, promoting the corrosion resistance of the materials [6–9]. Since then, many scholars have extensively studied the protection of surface oxide film, solution corrosion, and stress corrosion cracking of Fe–Mn–Al LDS. However, these results show

that the corrosion resistance of Fe–Mn–Al LDS is inferior to that of austenitic Ni–Cr stainless steel [9–15].

Recently, with more in-depth research on LDS, great progress has been made in the design of alloy composition, machining, and heat treatment of LDS, which realizes the differentiation of the microstructure, second phase, and properties of LDS, high-manganese TWIP steel, and TRIP steel with similar compositions [2, 5, 16–19]. Therefore, it is necessary to sort out the alloy composition design and microstructure of the current LDS and summarize past research on the corrosion resistance of LDS to guide the development of a new generation LDS with improved corrosion resistance.

### 1.1 Metallurgical Characteristic of LDS

The main function of Al in LDS is to reduce its density. The density decreases by  $0.098 \text{ g/cm}^3$  for ferrite with 1 wt% Al addition [1, 14]. According to a previous study on the Fe–Al phase diagram [20], three phases (disordered A2-phase ( $\alpha$ -Fe), ordered B2-phase (FeAl), and ordered DO<sub>3</sub>-phase (Fe<sub>3</sub>Al)) could be formed in the Fe–Al alloy. In the Fe–Al–C system, it is prone to produce  $\kappa$ -carbide when the Al content is higher than 5 wt% [21, 22]. The main role of C and Mn is to promote the formation of austenite phase. The density of austenite is  $8.15 \text{ g/cm}^3$ , which is higher than  $7.87 \text{ g/cm}^3$  of

Available online at <http://link.springer.com/journal/40195>.

✉ Xuequn Cheng  
chengxuequn@ustb.edu.cn

<sup>1</sup> Institute of Advanced Materials and Technology, University of Science and Technology Beijing, Beijing 100083, China

<sup>2</sup> National Materials Corrosion and Protection Data Center, University of Science and Technology Beijing, Beijing 100083, China

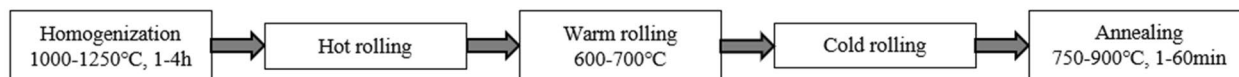
ferrite. However, the density of the austenite alloy decreases by  $0.101 \text{ g/cm}^3$  with adding 1 wt% Al, by  $0.41 \text{ g/cm}^3$  with adding 1 wt% C, and by  $0.0085 \text{ g/cm}^3$  with adding 1 wt% Mn [1, 14]. Mn and C introduce a variety of carbides into the alloy, among which  $\kappa$ -carbide is the most important. The main function of Ni is to strengthen the B2 phase and change it from the brittle inclusion to strengthening phase. The addition of Ni leads to a new B2 phase in NiAl [23]. Ni enhances the precipitation strengthening of the B2 phase and does not affect the original strengthening mechanism of  $\kappa$ -carbide [5].

LDS can be divided into ferrite LDS, duplex LDS, and austenite LDS according to the difference of alloying element content and microstructure type [24]. Few or only a few amount of Mn is added to ferrite LDS because of the expansion of the austenite phase zone of Mn [25–29]. Austenitic LDS can be divided into duplex LDS and austenitic LDS according to the different alloying elements and the second phase [5, 30–33]. The composition of duplex LDS is similar to that of austenitic LDS, but the final structure contains two phases of ferrite and austenite. The heat treatment and rolling processes of the three LDSs are shown in Fig. 1. For the alloy with Mn, Nb, and other carbide forming elements, a short time of intermediate annealing can be carried out before cold rolling, and then the final annealing can be carried out after cold rolling [25, 28]. The heat treatment method is also different according to the different second phases in austenitic LDS, as shown in Fig. 1b. The alloys strengthened by  $\kappa$ -carbides are usually annealed directly

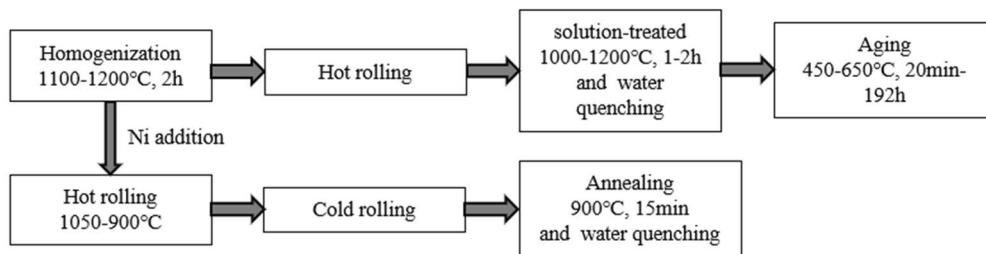
after hot rolling combined with a solution and aging treatment [20, 34–38]. The cold rolling and annealing process can also be added before the aging process [39, 40]. However, the alloy strengthened by the B2 phase is usually cold-rolled after hot rolling to refine the grain and then annealing [5, 36, 41]. For duplex LDS, it can also be annealed at  $1000 \text{ }^\circ\text{C}$  for 1 h after hot rolling [16, 32, 42–44]. The heat treatment of the duplex LDS with Ni addition is the same as that of the austenitic LDS with Ni addition [17, 45].

Temperature and time in the heat treatment can determine the distribution and morphology of precipitate. When heated at  $500 \text{ }^\circ\text{C}$ , the cellular transformation will take place and it can be described as  $\gamma \rightarrow \gamma + \kappa + \alpha$  [46]. When heated at  $600 \text{ }^\circ\text{C}$ ,  $\kappa$ -carbides could be formed in austenite ( $\gamma \rightarrow \kappa + \alpha$ ). With the heating temperature arriving  $800 \text{ }^\circ\text{C}$ , austenite with granular intragranular  $\kappa$ -carbide and nano- $\alpha$ -ferrite distributed at the austenite grain boundary could be observed in the alloy [47]. The  $\kappa$ -carbide transformation process at different heating time is similar to that at different heating temperatures. The difference is that the  $L_{12}$  phase ( $L_{12}$  is the metastable phase during the transformation from austenite to  $\kappa$ -carbide) in austenite will coarsen gradually with the extension of heating time. It will transform into lamellar intragranular  $\kappa$ -carbides under long-term annealing [48]. When annealed at  $700 \text{ }^\circ\text{C}$  for 100 h, the final microstructure will be a mixture of intragranular  $\kappa$ -carbides and intergranular  $\kappa$ -carbides. When annealed at  $800 \text{ }^\circ\text{C}$  for 100 h, the lamellar structure of intergranular  $\kappa$ -carbides can be observed in the

### a Ferritic LDS



### b Austenitic LDS



### c Duplex LDS

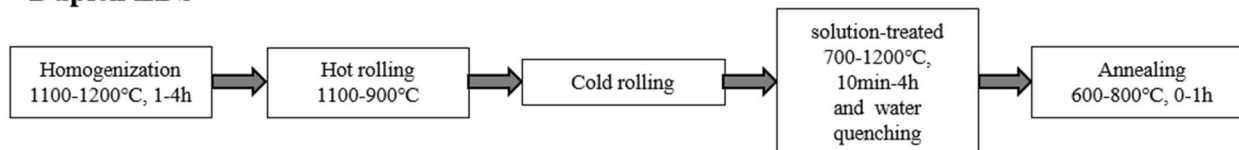


**Fig. 1** Typical heat treatment processes of **a** ferrite LDS [25–29], **b** austenitic LDS [5, 19, 30, 33–39, 41, 49], **c** duplex LDS [16, 32, 40, 42–45, 55]

final production [49, 50]. After cold rolling, the B2 phase in the steel is mainly a stringer band along the rolling direction. This stringer band B2 phase has higher brittleness and poor ductility [17]. The annealing time will also affect the distribution of the B2 phase.

The influence of alloying elements and microstructures on LDS properties in metallurgical process is diverse. However, due to the basic content of Fe, Mn, and Al in LDS, different kinds of LDSs have common performance in corrosion resistance. The chemical composition, microstructure types, and precipitate characterizations (variety, size, and amounts) have a significant effect on the corrosion resistance of the LDS, which will be discussed detailedly in the following.

## 1.2 Microstructure and Mechanical Properties

### 1.2.1 Ferritic LDS

Ferritic LDS mainly contains  $\delta$ -ferrite, FeAl (B2 phase), and  $\text{Fe}_3\text{Al}$  (DO3 phase) [51]. As the APT (atom probe tomography) maps of the rolled structure and element distribution shown in Fig. 2a,  $\kappa$ -carbides can also be formed when Mn is added [20]. The ferritic LDS is mainly made of single ferrite with the amplification effect of Al on  $\delta$ -ferrite phase zone. The higher Al content increases the recrystallization

temperature of ferrite. This would promote the ferrite to be elongated into ribbons along the rolling direction during the hot rolling process (Fig. 2b) [25, 26]. Cold rolling and annealing could promote the formation of equiaxed crystals and eliminate the adverse effects of high Al content (Fig. 2c) [25]. To avoid the formation of hard and brittle  $\text{Fe}_3\text{AlC}_{0.5}$  precipitates, the C content should be lower [26]. The addition of strong carbide forming elements (such as Nb) is an important strengthening method for ferrite LDS, which can facilitate the carbide particle precipitation at the ferrite grain boundary (Fig. 2d) [28]. The addition of Nb can also inhibit the recrystallization of ferrite during hot rolling and improve the mechanical properties of ferrite LDS (Fig. 2e) [14, 25, 26, 28, 29]. Due to the limitation of mechanical properties, the research progress regarding the corrosion resistance of ferritic LDS is relatively lacking, and no systematic research has been reported.

### 1.2.2 Austenitic LDS

There are two different design philosophies for austenitic LDS: one is to add a large amount of Mn (> 10%) to form  $\kappa$ -carbide [30, 31, 36, 52], and the other is to add Ni (0–5%) to form the B2 phase [2, 5]. Different design methods

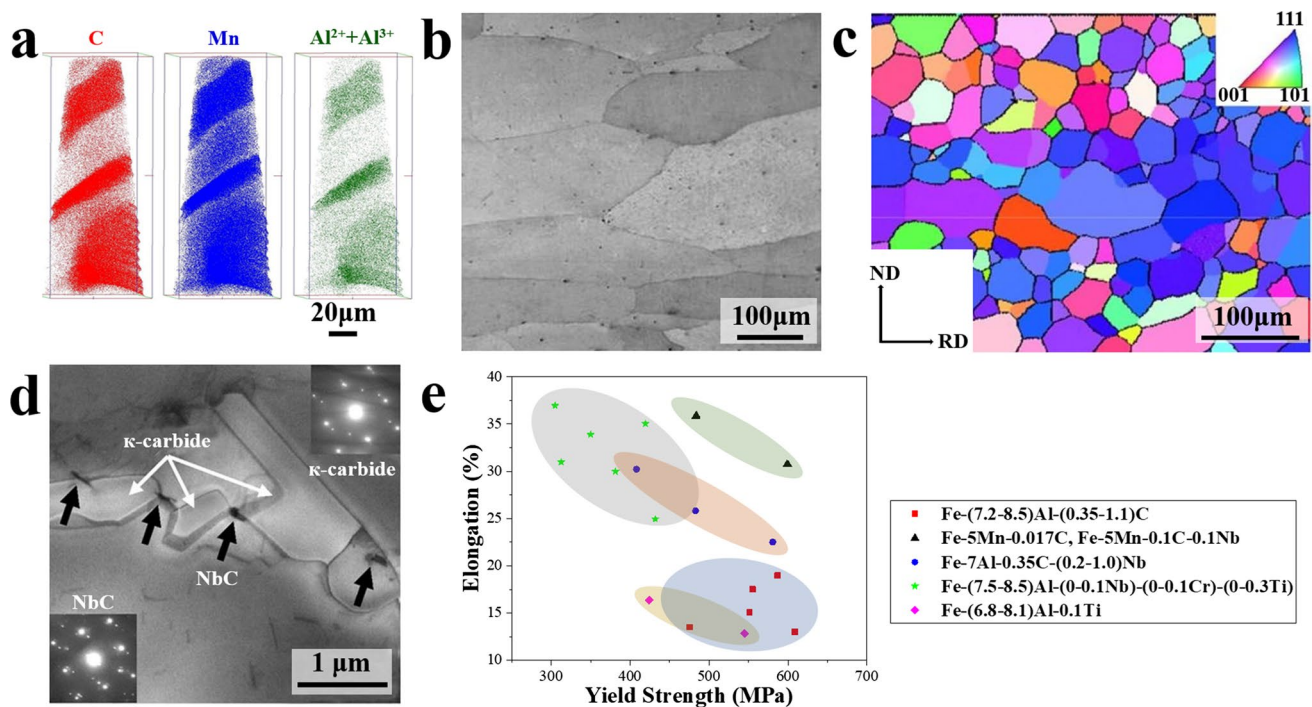


**Fig. 2** a APT maps of C, Mn, and Al for Fe-3.2Mn-10Al-1.2C [51], b characteristics of the optical microstructures of Fe-7Al in hot-rolled condition [26], c IPF maps of Fe-8Al-5Mn alloy after cold rolling and annealing at 750 °C for 1 h [28], d TEM micrograph of NbC and  $\kappa$ -carbide along grain boundary of Fe-8Al-5Mn-0.1Nb-0.1C [28], e statistical of mechanical properties of ferrite LDS with different compositions [14, 25, 26, 28, 29]

influence the microstructural and mechanical properties of the austenitic LDS (Fig. 3).

The spatial distribution of  $\kappa$ -carbides in austenite and the composition change at the interface between them are shown in Fig. 4a and b [31]. The  $\kappa$ -carbides observed in austenitic LDS during 500–1200 °C heat treatment are generally divided into intragranular and intergranular  $\kappa$ -carbides. The TEM dark-field micrographs and selected-area diffraction patterns of intergranular  $\kappa$ -carbide and intragranular  $\kappa$ -carbide are shown in Fig. 4c and d [35].

B2 phase ((Fe, Mn, Ni)Al) and DO3 phase ((Fe, Mn)<sub>3</sub>Al) could be formed in LDS. The formation of the stringer band B2 phase is a unique phenomenon in LDS with Ni addition [2, 5]. Annealing can change the morphology of the B2 phase, which can be divided into three types: (1) retained stringer bands, (2) 200–1000-nm particles, and (3) 50–300-nm ultrafine particles [2]. The discontinuous nanoscale B2 phase can act as a pinning dislocation, thus changing the damage of the previous stringer band morphology to ductility [18]. The orientation relationship between fully recrystallized austenite and B2 phase is shown in Fig. 5a. The matrix has been fully recrystallized after long-time annealing. Most of the B2 particles are located at the austenite grain boundary, and only a few are located in the austenite grains, as indicated in Fig. 5b and c [5, 53]. There are also nano-sized  $\kappa$ -carbides and DO3 phases in the austenite matrix and B2 phase particles, respectively.

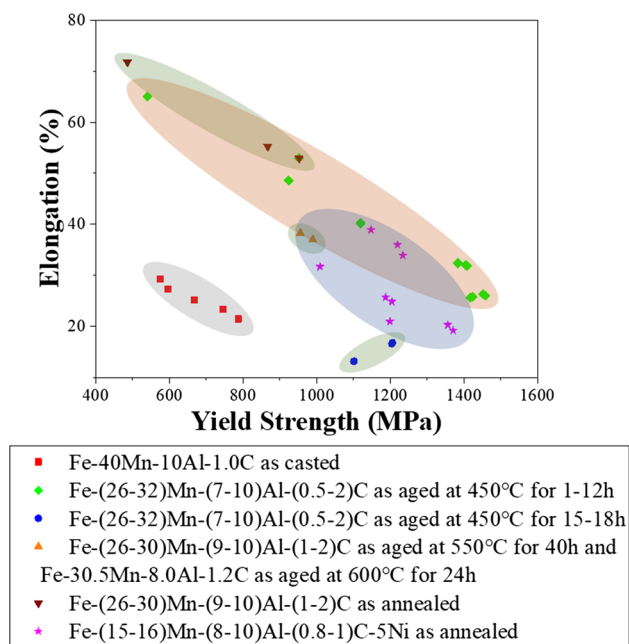


**Fig. 3** Statistical of mechanical properties of ferrite LDS with different compositions and different heat treatments [2, 5, 21, 30, 34, 36–39, 41, 49, 53]

It is worth mentioning that the premise of introducing B2 phase strengthening is to control the B2 phase in fine size and dispersion distribution, since the larger B2 phase in steel will still affect the properties of LDS and become the origin of cracks and SCC (stress corrosion cracking) [54]. Due to the effect of B2 on the corrosion resistance of materials, precipitates controlment will be an important factor to improve the corrosion resistance of materials in the future.

### 1.2.3 Duplex LDS

In the duplex LDS, the microstructure after hot rolling is a  $\delta$ -ferrite band along the rolling direction and austenite refined owing to high-temperature recrystallization (Fig. 6a) [44]. The coarse-grained  $\kappa$ -carbides in the hot-rolled microstructure correspond to the Mn-rich region, whereas the ferrite corresponds to the Mn-poor region [55]. The temperature and time of solution treatment can change the morphology of  $\delta$ -ferrite. When solution treatment is carried out at 800–900 °C, the  $\delta$ -ferrite is locally coarsened from a strip shape to a bamboo shape [44]. When the temperature is higher than 1000 °C, the matrix is mainly composed of bulk  $\delta$ -ferrite, and the content of austenite decreases significantly. After annealing at 800–900 °C, the  $\kappa$ -carbide will change from lamellar to polygonal block, ferrite will also change to polygonal grains, while austenite grains tend to coarsen [32, 43].

In addition to the idea of forming  $\kappa$ -carbides for strengthening, the methods of adding Ni to form B2 phase and adding Cr to improve the corrosion resistance are also developed. The effect of alloying elements on mechanical properties of duplex LDS is shown in Fig. 6b. In a word, the composition design is mainly used to increase the content of austenite phase. In the process of deformation, slip band can be formed in austenite grains, and the existence of a large amount of austenite can also promote the formation of dislocation substructure (Fig. 6c) [32]. This will improve the ductility of duplex LDS and relieve the internal strain energy during hot rolling to improve the strain hardening rate.

The complexity of structure leads to the sensitivity to local corrosion in duplex LDS. Transgranular cracks are easier to pass through the ferrite region and terminate in the austenite region [10]. Therefore, it will be an important research direction to control local corrosion such as SCC in duplex LDS by regulating the final structure.

## 2 Surface Oxidation of LDS

### 2.1 Oxidation in Hot Corrosion

In the metallurgical process of LDS, heat treatment is necessary for promoting the passive film formation on the surface

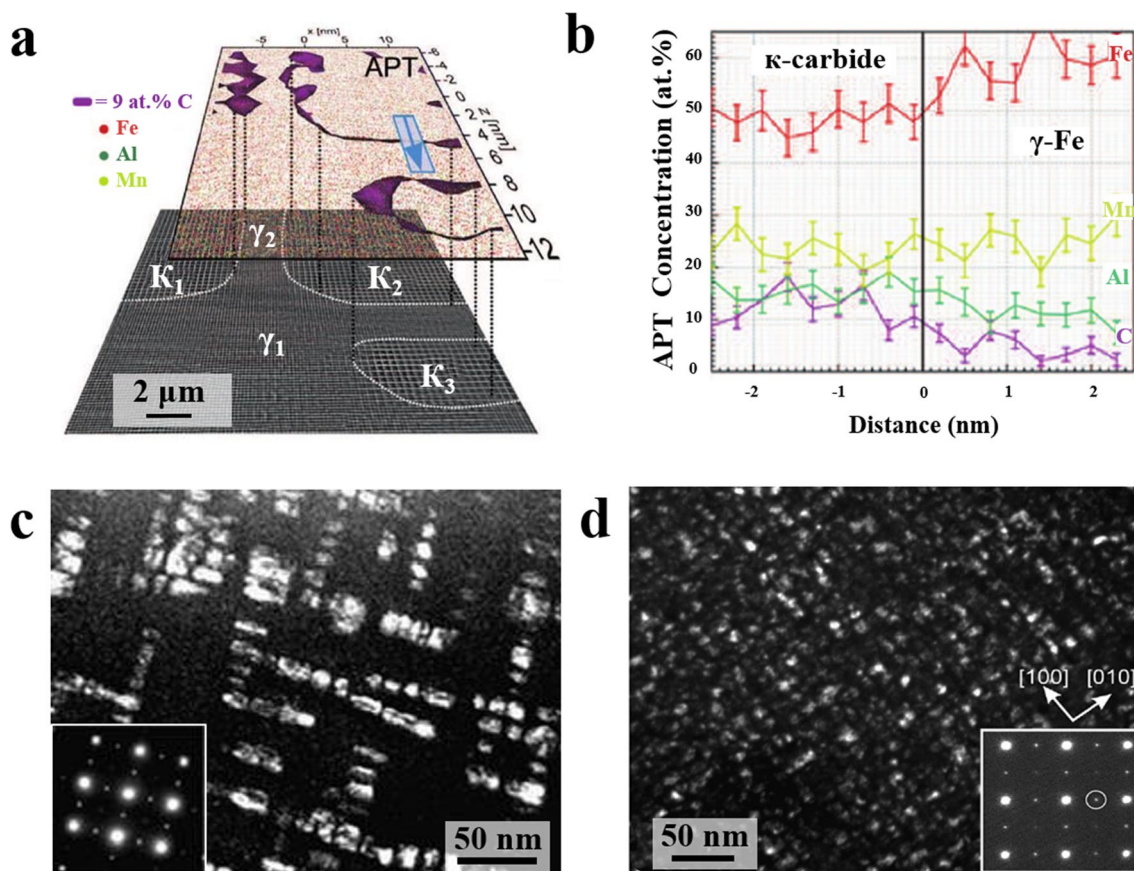


**Fig. 4** **a** Direct 1:1 correlation of atomic resolution STEM and APT of Fe-26.7Mn-14.0Al-5.3C alloy, **b** APT concentration profile extracted across the horizontal  $\gamma/\kappa$  interface highlighted by the arrow in **a** [31], TEM dark-field micrographs and selected-area diffraction patterns of **c** Fe-28Mn-9Al-0.8C alloy aged at 625 °C for 3 h and **d** Fe-25.7Mn-10.6Al-1.2C alloy [35]

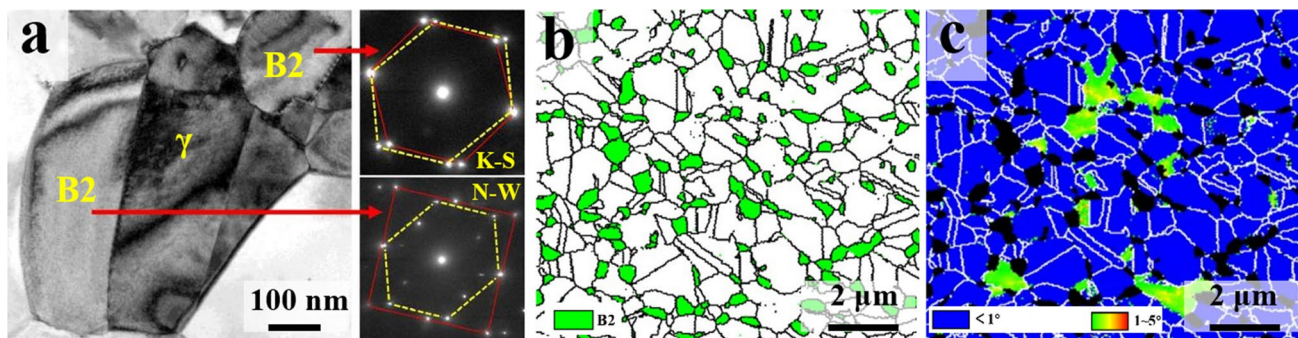


**Fig. 5** **a** TEM bright-field image and corresponding SADPs of austenite and B2 in Fe-21Mn-10Al-1C-5Ni alloy, EBSD phase map **b** and KAM **c** of austenite grains in Fe-21Mn-10Al-1C-5Ni alloy annealed at 900 °C for 15 min [5]

that improves the corrosion resistance of LDS. In a high-temperature gas service environment (above 600 °C) with gas state corrosive ions ( $\text{Cl}^-$ ), LDS exhibits better corrosion resistance property [56]. The surface of the formed LDS has a double-layer structure: the outer oxide scale is composed of  $\text{Mn}_2\text{O}_3$ ,  $\text{Fe}_2\text{O}_3$  and  $\text{Mn}_3\text{O}_4$ ; the inner oxide scale is mainly

composed of  $\text{Al}_2\text{O}_3$ , and the porosity of the alloy substrate is mainly due to the migration of Mn to the outer oxide scale after selective oxidation. Additionally, some of the pores are formed by the infiltration of  $\text{Cl}^-$  into the interior to form  $\text{AlCl}_3$  (Fig. 7a) [57]. In the  $\text{Cl}^-$ -containing environment, these voids are conducive to the migration of  $\text{Cl}^-$ , making

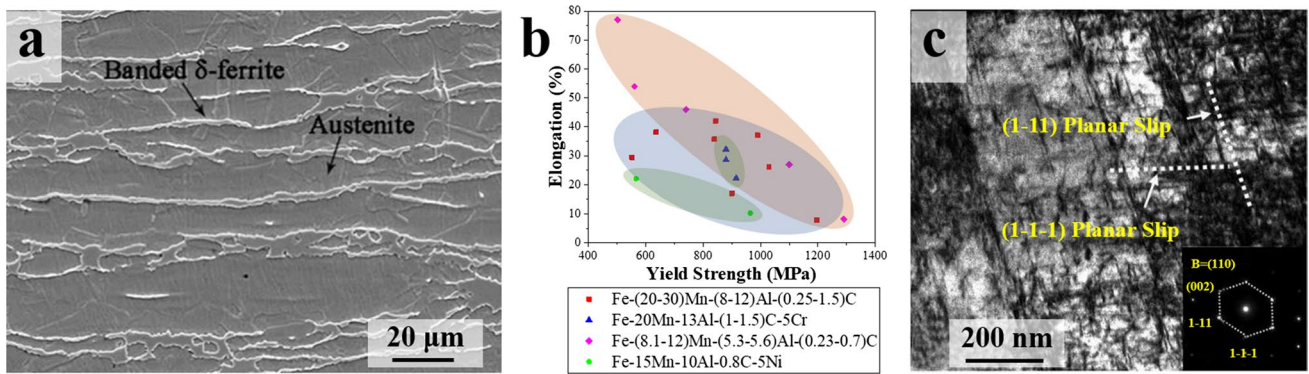


**Fig. 6** **a** Microstructure of Fe-26Mn-6.2Al-0.05C steel after hot rolling at 900–1100 °C [44], **b** statistical of mechanical properties of duplex LDS with different compositions [5, 16, 32, 40, 42–45], **c** TEM bright-field images of Fe-15Mn-7Al-0.8C alloy tensioned at strains of 5% and 10% [32]

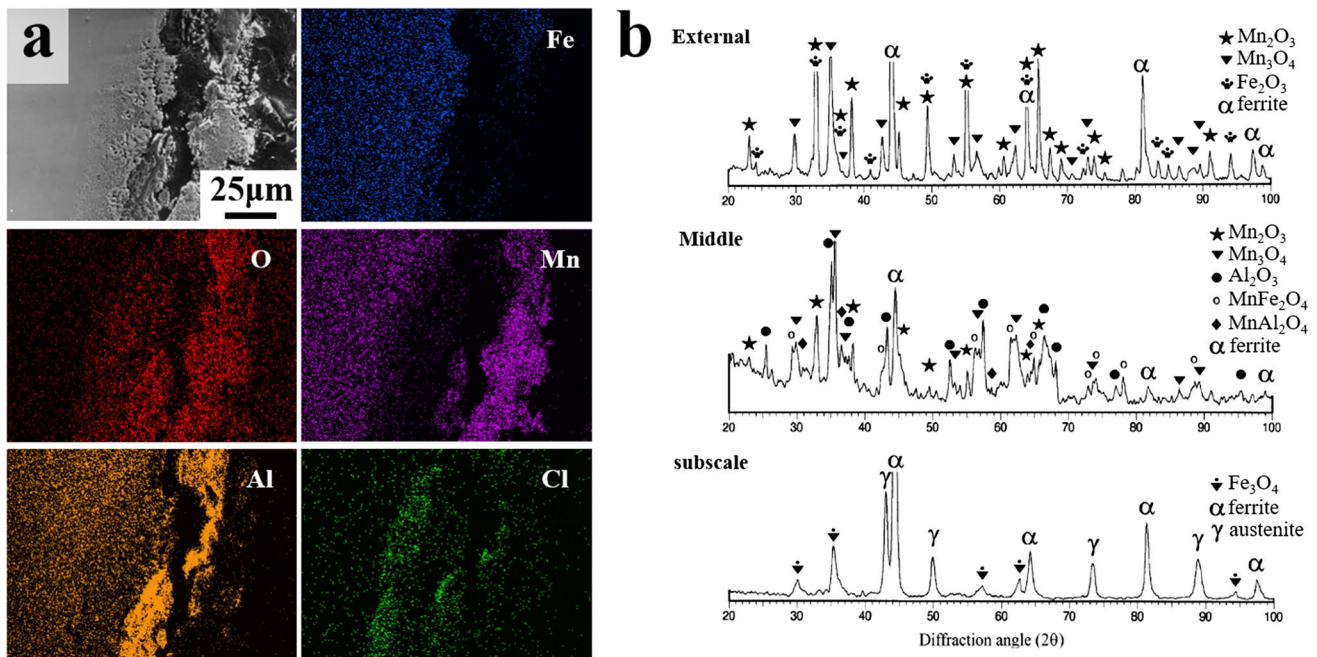


**Fig. 7** **a** Microstructure and EDX maps of Fe-31.1Mn-9.07Al-0.89C alloy corroded at 750 °C for 4 h, **b** XRD analyses of scale formed on Fe-30.1Mn-8.05Al-0.88C-3.04Cr alloy corroded at 850 °C for 24 h [56]

the alloy matrix more susceptible to corrosion [56]. There are two critical Al content values for Al-containing alloys [58]. The first critical Al content is 3.85–4.84 at%, which indicates that the alloy changes from internal oxidation to external oxidation. The second critical Al content is 13.3–14 at%, which indicates that the surface oxidation products change from Fe-Al mixed oxide to  $\text{Al}_2\text{O}_3$ . In this condition, the alloy surface is completely protected by a passive film. Therefore, the addition of Al can provide a better high-temperature corrosion resistance in the hot working temperature range for LDS. Secondary ferrite is usually associated with the formation of voids [56], which may also act as nucleation

sites for pitting corrosion. Refine grains formed in the cold rolling process can increase the concentration of the cation diffusion interface and improves the surface oxidation at high temperatures. In the initial process of high-temperature oxidation, the fine grains are conducive to the outward diffusion of cations. This could also prevent the inward oxidation expansion of  $\text{Mn}^{2+}$  and enhance the inward oxidation expansion of  $\text{Al}^{3+}$  [59]. Unstable or metastable oxides like MnO and FeO appear only in the surface oxide scales, and the structure of the  $\text{Al}_2\text{O}_3$  film in the inner oxide layer formed by fine-grain LDS is more compact and continuous [59]. In this environment, the corrosion resistance of the alloy surface

will be improved with an increase in Al content [57]. Cr has no obvious influence on the corrosion resistance enhancement in this condition, due to the volatile salts (like  $\text{Na}_2\text{CrO}_4$  and  $\text{CrCl}_2\text{O}_2$ ) in  $\text{Cl}^-$ -induced hot corrosion [56]. This is the reason for no Cr-containing salts detected in the oxide layer components (Fig. 7(b)).

## 2.2 Passivation and Electrochemical Control in a Liquid Environment

The passivation behavior of LDS is closely related to the type of solution medium. The corrosion resistance of LDS in  $\text{Cl}^-$  environments can be enhanced by anodic passivation. In a 50%  $\text{HNO}_3$  solution, Fe-31Mn-8Al alloys can be passivated [60]. Generally, the passivation of the LDS film for 300 min can effectively improve the corrosion resistance of the passivation film [61]. A significant passivation zone could be seen in the passivation curve owing to the high passivation of Al and Cr and the oxidation of the 50%  $\text{HNO}_3$ . In a 10% HCl solution, the alloy with Al or Cr addition has no passivation behavior, whereas the alloy can spontaneously passivate in 10%–50% NaOH solution [60, 62]. As shown in Fig. 8a, in 3.5 wt% NaCl solution, passivation will appear in LDS alloys with Al content higher than 5% [13, 62]. In  $\text{NaSO}_4$  solution, LDSs with different Al contents can be spontaneously passivated [63]. The critical passivation current density ( $I_{\text{CR}}$ ), critical passivation potential ( $E_{\text{CR}}$ ), and passivation current density ( $I_p$ ) will decrease along the increase in Al content [63]. In a 0.5 mol/L  $\text{H}_2\text{SO}_4$  solution, LDS showed passivation only at pH 5.55–6.10 [9]. In rainwater, LDS with Al content greater than 5% tends to be passivated [63], and the passivation behavior of LDS in this medium remains to be studied.

The composition and structure of the alloy are also important factors that affect the electrochemical properties. Cr is an important passive film-forming element. The enrichment

of  $\text{Cr}_2\text{O}_3$  in passivated film increases with the increase in Cr content [64]. From the interaction of Cr with other elements, the mixed addition of Cr and Al will reduce the critical Al content. This allows the alloy surface to be completely covered by the passive film and reduces the nucleation of Fe oxide, making the passive film more uniform to improve the corrosion resistance (Fig. 8b) [58]. Moreover, Cr can change the passive film structure, which is reflected by the limitation of Mn, the enrichment of Al in the passive film, and the thickening of the passive film [61]. Mo has a similar influence to Cr in limiting the entry of Mn into the passive film and enriching the Al content in the passive film [65]. The unique function of Mo is to improve the stability of passive films [65] by being incorporated into the passive films in the form of various oxides, such as  $\text{Mo}_2\text{O}_3$ ,  $\text{MoO}_2$ , and  $\text{MoO}_3$  [66, 67]. The addition of Cr and Mo mixture into LDS can prolong the rupture time of passive film as shown by the phase angle platform in Fig. 8c. Mn is generally considered detrimental to LDS surface oxidation. With Mn content increase, the amount of Mn oxide in the outermost oxide layer of the alloy will gradually increase. This results in a destruction of the passive film continuity and derogates the corrosion resistance of the alloy [68]. However, some positive effects of Mn on corrosion resistance have been reported. Mn on the alloy surface will be selectively dissolved in a corrosive ionic solution, which leads to the enrichment of Al on the alloy surface, promotes the growth of the passive film, and makes the structure of the passive film more compact [64].

The increase in Al and Cr content in LDS can result in an  $E_{\text{corr}}$  increase and  $I_{\text{corr}}$  decrease in the acidic solution (Fig. 9a, b). Similar effect on the LDS has also been reported in  $\text{NaSO}_4$ , NaCl, and rainwater solutions [13, 63]. With an increase in the Mn content in LDS, the oxidation tendency of Mn increases. However, it is not conducive to the formation of a uniform passivation film containing Al

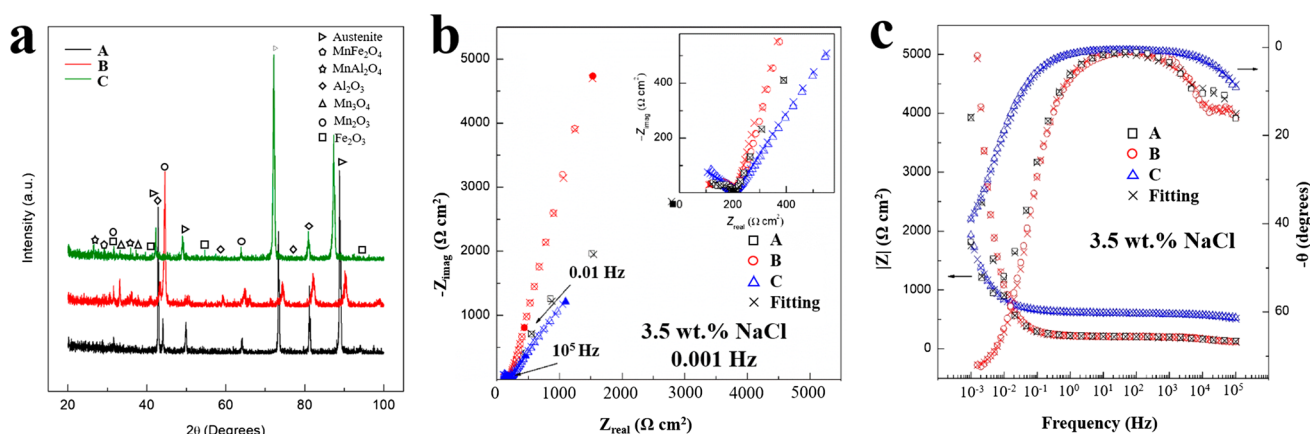


**Fig. 8** Three alloys (A: Fe-22.6Mn-6.3Al-3.1Cr-0.68C, B: Fe-28Mn-5.2Al-5.1Cr-2.8Si-0.95C, C: MBIP) (Fe-30Mn-8.5Al-3.2Cr-1.1C) in 3.5 wt% NaCl solution of **a** XRD pattern of surface corrosion products, **b** Nyquist plots, **c** Bode plots [62]

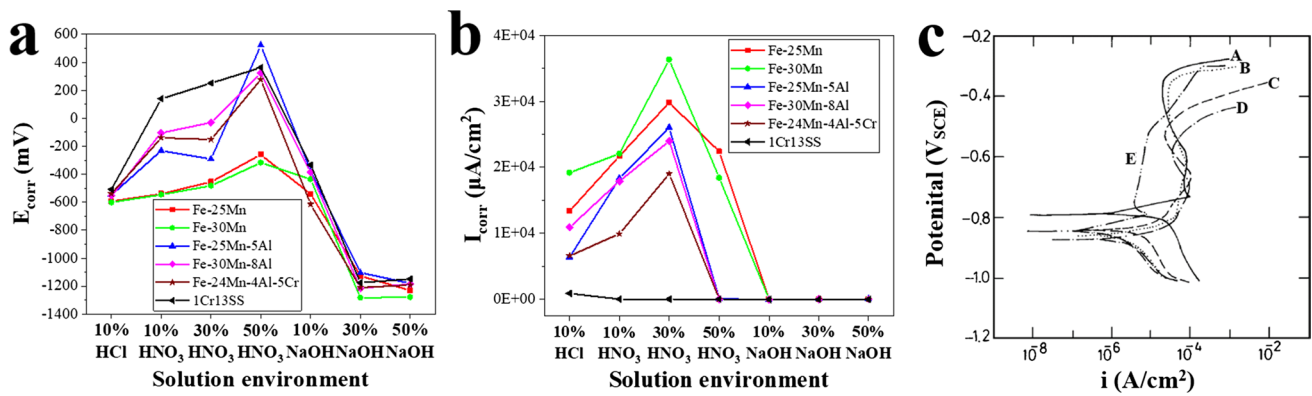


**Fig. 9** Effect of alloying elements and solution environment on **a**  $E_{\text{corr}}$  and **b**  $I_{\text{corr}}$  in LDS [60], **c** potentiodynamic polarization curves of the five Fe–Mn–Al alloys (A–Fe-28.52Mn-9.97Al-1.047C, B–Fe-29.6Mn-10.19Al-0.832C, C–Fe-28.63Mn-10.45Al-0.498C, D–Fe-29.99Mn-10.19Al-0.305C, and E–Fe-21.5Mn-9.86Al-0.33C-6.32Cr) in deaerated 3.5% NaCl solution [11]

and Cr. Moreover, increase in Mn promotes the kinetics of the anodic reaction and leads to an  $E_{\text{corr}}$  decrease,  $I_{\text{corr}}$  increase, and polarization resistance decrease [68].  $E_{\text{corr}}$  was influenced by the synergistic effect of these elements. It can be assumed that 5% Al can counteract the damage of 25% Mn to corrosion resistance [13, 56, 60, 61, 63, 64, 69, 70]. In the Cl<sup>-</sup> environment, the width of the passivation zone decreases with an increase in the ferrite content. The Mn content has an obvious effect on the ferrite content. As shown in Fig. 9c, the dual-phase LDS with a higher ferrite content exhibits almost no passivation behavior because of the lower Mn content [11].

### 3 Localized Corrosion of LDS

#### 3.1 Pitting Corrosion of LDS

The corrosion resistance of LDS was closely related to the microstructure, which was adequately impacted by hot rolling. Owing to the discontinuity alloy structure formation along the rolling direction after hot rolling, the stability of passive film reduced and the probability of pitting corrosion increased [71]. Cr and Mo are important alloy elements for inhibiting pitting corrosion. In the Fe–Mn–Al–C alloy, the pit number ratio and pit area on the surface area decreased with the Cr content increase (Fig. 10a–d) [72]. As shown in Fig. 10e, the increase in Cr can also result in an  $E_{\text{pit}}$  increase [73], which is considered to be realized by the effect of Cr and Mo on protective oxide in passive film [72, 74]. As passivation film XPS result shown in Fig. 10(h), Mo and Cr are gradually enriched from the outside to the inside of the passive film. As shown in Fig. 10g, LDS has the best pitting corrosion resistance with 3% Cr and 3% Mo addition. With the synergistic effect of Cr and Mo, a protective passive film could be formed on the LDS surface, which can

facilitate the alloy pitting corrosion resistance [73]. However, the content of Cr should be strictly limited, since the corrosion resistance and mechanical properties will decline when the Cr content is more than 8%. The hysteresis loop of cyclic polarization curve will also increase with the Cr content increase, which means that the re-passivation ability of the alloy will be decreased. As shown in Fig. 10f, LDS with 9% Cr addition will be not passivated after pitting, resulting in an increase in pitting sensitivity [72]. Cr<sub>7</sub>C<sub>3</sub> precipitates formed in the LDS will reduce the pitting potential [73]. Excessive addition of Mo or Cr will make DO3 ordered phase become the starting point of pitting, which will adversely affect the pitting resistance. When the content of Cr and Mo is more than 3%, it promotes the pitting corrosion of the interface between DO3 and austenite, as shown in Fig. 10i [65, 75].

#### 3.2 Stress Corrosion Cracking (SCC) and Hydrogen Embrittlement of LDS

The second phase formed during the heat treatment has signal influence on the strength and environmental corrosion fracture of LDS. The decomposition of austenite in steel during heating can be divided into two stages. The first stage is the decomposition of austenite into  $\alpha$ -ferrite and  $\kappa$ -carbide.  $\kappa$ -carbides are considered as hydrogen capture sites [76], and the capture diffusive hydrogen ability of  $\kappa$ -carbide depends on the content of C and Mn. The C content determines the number of vacancies in the  $\kappa$ -carbides, while the Mn content determines the total trapping efficiency. Therefore, the decrease in C content and the increase in Mn content in  $\kappa$ -carbide precipitates can reduce the probability of hydrogen embrittlement in LDS [77]. The second stage is the partial decomposition of austenite into  $\beta$ -Mn, and in this stage austenite coexisted with  $\beta$ -Mn. The  $\beta$ -Mn phase tends to become the origin of the crack [78].



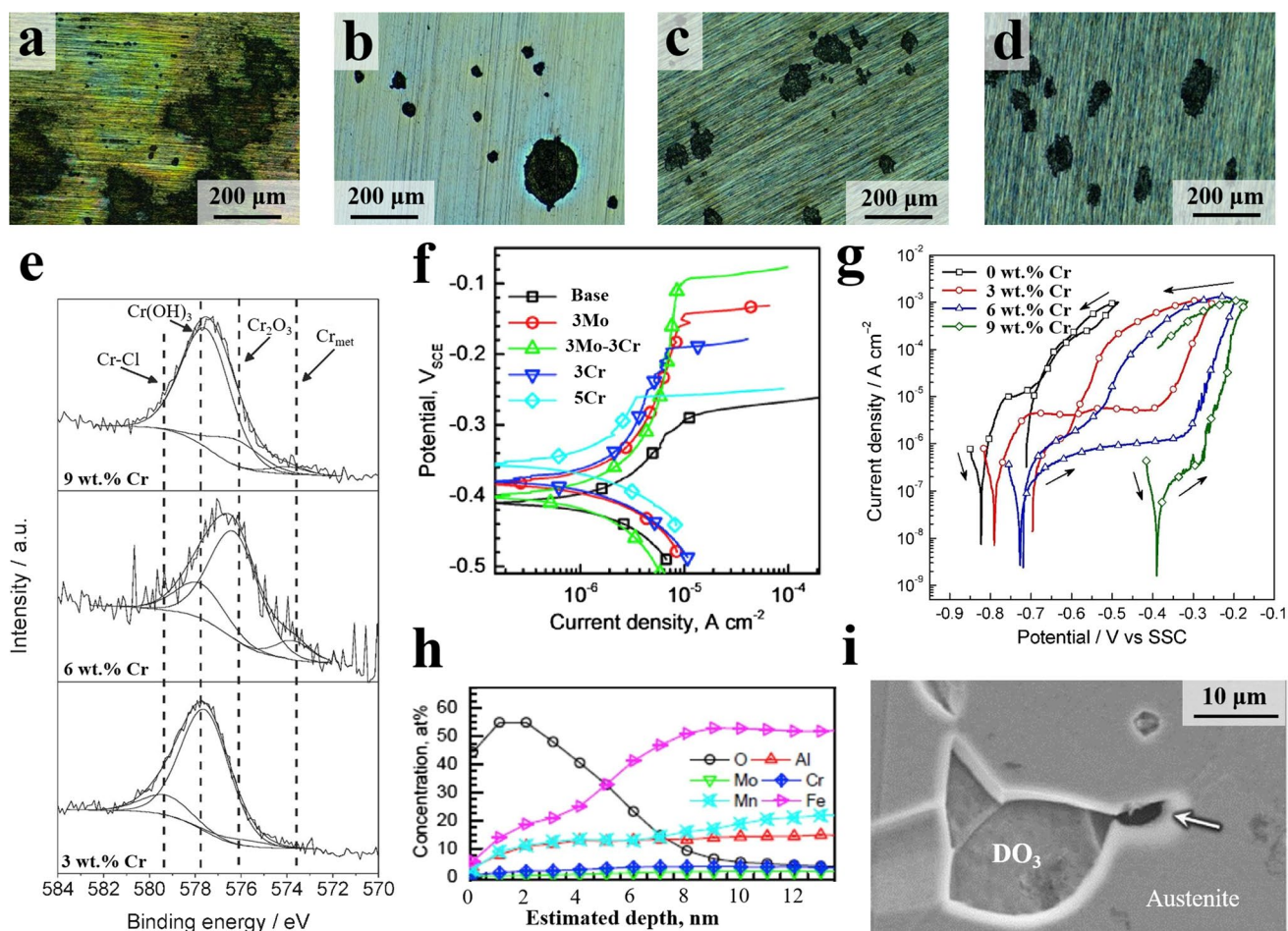


**Fig. 10** Pitting corrosion morphology of Fe-30Mn-5Al-0.5C (a) and Fe-30Mn-5Al-0.5C-3Cr (c) 6Cr (d) 9Cr steels after hot rolling and immersion in 0.1 M NaCl solution for 30 min [72], e cyclic polarization curves for thermo-mechanical processed Fe-30Mn-5Al steel in deaerated 0.1 M NaCl solution and f XPS spectra for Cr  $2p_{3/2}$  of Fe-30Mn-5Al steels with 3, 6, and 9 wt% Cr [72], g polarization curves of Fe-29.8Mn-10.7Al-1.13C-XMo-XCr steels measured in a 0.6 M NaCl solution, h chemical composition depth profiles in the passivated layers of 3Mo-3Cr alloys, and i pit initiation sites of Fe-29.2Mn-10.6Al-1.13C-5Cr [65]

As shown in Fig. 11a, the fracture of LDS is transgranular quasi cleavage with some large flatter facets in a  $\text{Cl}^-$  containing environment. The fracture in Fig. 11a is flatter than that in Fig. 11b. The tearing ridge is in austenite, and the flat zone is in ferrite on the surface of the fracture. Hence, ferrite has a higher SCC sensitivity than austenite. This indicates that SCC is more likely to occur in dual-phase LDS than ferrite LDS in a  $\text{Cl}^-$  environment [10].

In a  $\text{Cl}^-$  environment, when the anode potential is applied to LDS, the fracture surface shows cleavage transgranular fracture, and there are some pits around it. In this condition, SCC is not likely to occur [12]. The SCC will be displayed in LDS when a negative cathode potential value ( $\leq -1000$  mV) is applied, and the fracture morphology and fracture path are shown as intergranular fractures (Fig. 11(c and d)). This is attributed to the fact that the cathodic reaction is a hydrogen evolution reaction [68], which promotes the cathodic reaction kinetics to increase the sensitivity of LDS to hydrogen

embrittlement [79]. The casting defects in LDS can also be the origin of cracks in the  $\text{Cl}^-$  environment (Fig. 11e [12]). In the constant load test in  $\text{Cl}^-$  environment, LDS barely shows SCC behavior. However, in the slow strain-rate test, SCC easily occurs [80]. This might be related to the continuous production of exposed metal surface during the large-scale plastic deformation process, and the continuous absorption of hydrogen in the alloy matrix during strain increases will exacerbate the SCC risk [79]. When SCC occurs, the fracture is composed of transgranular and intergranular fractures in different microstructures. The crack extends vertically in the direction of the loading. The transgranular fracture is adopted in the ferrite area to pass through the ferrite grain, and it is cut off in the austenite area or along the austenite/ferrite interface, as shown in Fig. 11f.

The diffusion rate of hydrogen in austenite is six orders of magnitude slower than that in ferrite at room temperature, and the hydrogen solubility in austenite is also higher than

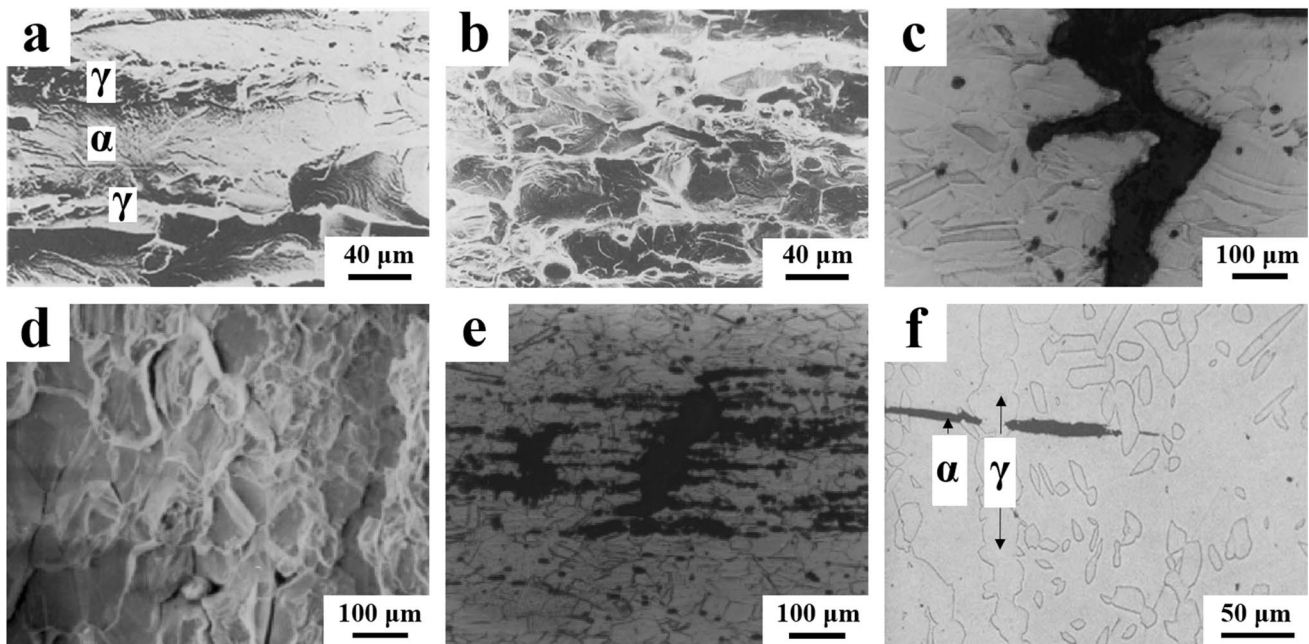


**Fig. 11** Fractographs of alloy **a** Fe-27.7Mn-8.9Al-0.42C in 3.5% NaCl and **b** Fe-24.4Mn-9.96Al-0.4C in 3.5% NaCl [10], **c** intergranular secondary crack in alloy Fe-32.16Mn-9.41Al-0.93C applied potential of  $-1,200$  mV, **d** fracture surface of alloy Fe-32.67Mn-9.42Al-0.91C at  $-1,300$  mV in 3.5% NaCl solution [12], **e** cracks caused by corrosion at material defects in Fe-31.3Mn-8.8Al-0.9C alloy [12], **f** side surface of cracks in Fe-27.7Mn-8.9Al-0.42C alloy in 3.5% NaCl solution [10]

that in ferrite [81]. This reduces the possibility of hydrogen embrittlement in austenitic LDS [82]. As shown in Fig. 12a, the  $\text{Al}_2\text{O}_3$  protective layer can prevent hydrogen absorption in aqueous solution environments [83, 84]. The typical mechanism of hydrogen-assisted cracking in LDS is grain boundary triple junction cracking, which is caused by hydrogen localization near grain boundary triple junctions (Fig. 12b and c) [85]. As a weak trap of hydrogen, Al atoms can change the arrangement of atoms around it and cause local expansion while adsorbing hydrogen atoms, which in turn promotes its own adsorption of hydrogen atoms [86]. After adding 1.5 wt% Al to LDS, the permeability and diffusivity of hydrogen in LDS will be reduced by 35%. The solubility of hydrogen in LDS will be increased, which means that the addition of Al will enhance the hydrogen embrittlement resistance of LDS [87]. Hence, with the increase in Al content, SCC will be prevented because dislocation sliding on the slip surface around the crack tip is necessary for crack initiation and propagation, and Al can reduce dislocation mobility [82]. For the cathodic reaction, an increase in the Mn content will lead to a decrease in the catalytic performance of the hydrogen evolution reaction, resulting in a decrease in the cathodic reaction rate and a reduction in the hydrogen embrittlement sensitivity of the alloy. For the anodic reaction, a Mn content increase will lead to an increase in the oxidation tendency of manganese, hence increasing the anodic reaction rate [68]. Cr, Mo, and Si can

reduce the sensitivity of LDS to hydrogen embrittlement in  $\text{Cl}^-$  environments, but Si will increase the SCC sensitivity of LDS in  $\text{Cl}^-$  environments, which cannot change the SCC mechanism of LDS [12].

#### 4 Future research on the Corrosion Resistance of LDS

Currently, the main researches of LDS are focused on the mechanical properties. The corrosion mechanism and corrosion resistance research are not sufficient. There is still a chasm in the corrosion resistance research of LDS:

1. Under the limitation of the LDS mechanical properties, the research on corrosion resistance of this material has not been widely spread, resulting in the cognitive limitations. In particular, there are gaps in the understanding of corrosion mechanisms of LDS in different types of environments. In the early studies, the single macro-electrochemical approaches hindered our understanding of the corrosion initiation mechanism at micro-nanoscales. With the research progress of mechanical properties, the popularization and application possibilities of such material have been greatly enhanced. In more abundant service environment, investigating the corrosion mechanism of LDS with advanced microelec-

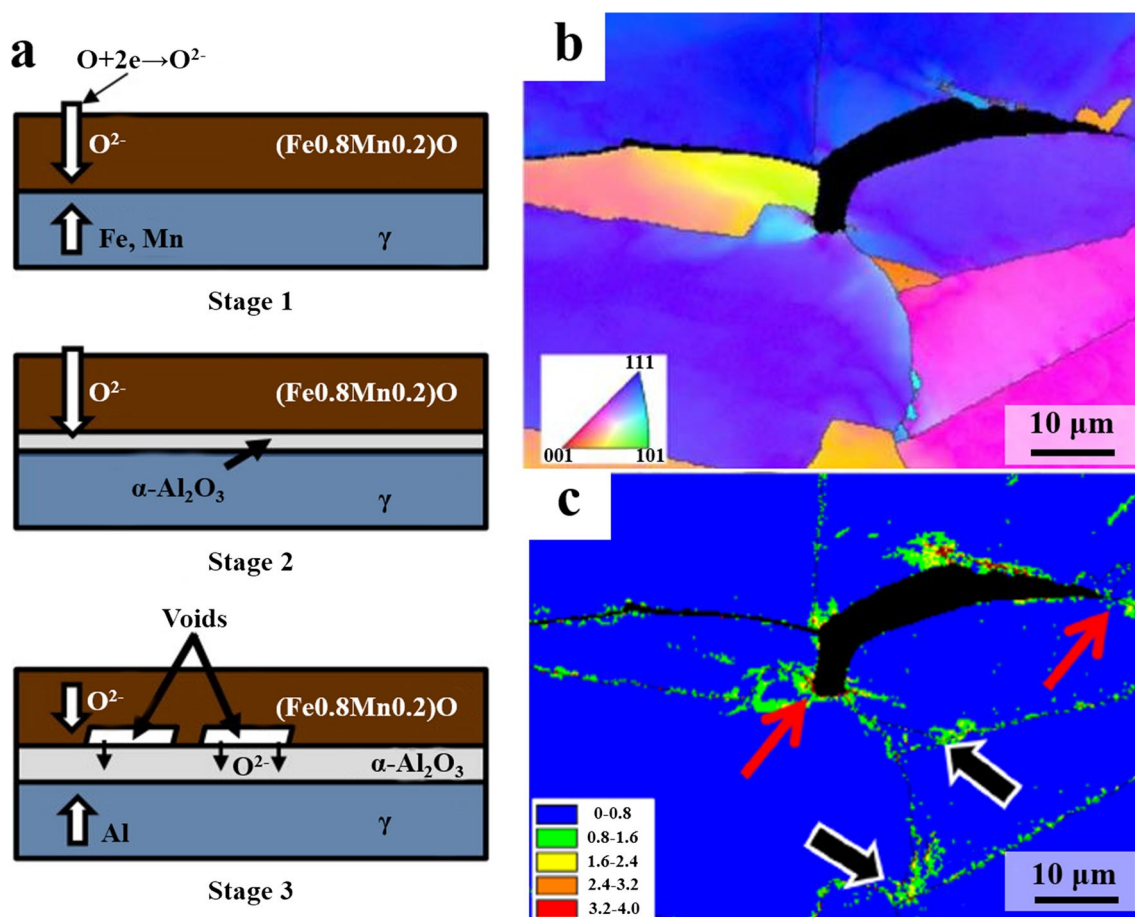


**Fig. 12** **a** Formation mechanism of the oxide formation in Fe–Mn–Al steels during hydrogen charging [84], **b** RD-IPF map, and **c** KAM map of hydrogen-related subcracks caused by slip localization in Fe-25.7Mn-10.6Al-1.16C alloy [85]

trochemical technology will be helpful to improve the performance of such LDS. In the future research work, the synergistic effects of materials characteristic (alloy variety, microstructure, precipitates, and the passive film) and environment characteristic (medium variety, corrosive ion concentration, temperature, and pH) in its corrosion process are necessary.

2. The limited literature mainly focuses on the pitting corrosion and SCC behavior on the LDS. The complicated microstructure characteristic (chemical alloy compound, inclusions, carbides, precipitates, high density dislocation, passive film) might have a remarkable influence on the localized corrosion (pitting corrosion, crevice corrosion, intergranular corrosion, galvanic corrosion, corrosion fatigue, and hydrogen stress corrosion) of LDS. The research about the chemical and electrochemical process in different localized corrosion of LDS under different service environment will be helpful to improve the cognition of the LDS properties.
3. Microalloying is an important method to improve the corrosion resistance of materials. On the basis of obtain-

ing good strength and toughness of LDS, the influence of different corrosion resistance elements (such as Cr, Ni, Mo, Cu, and rare earth) on the LDS corrosion resistance needs to be further systematically investigated. This would make a positive impact on revealing the influence mechanism of these microalloying elements on the LDS corrosion resistance.

Therefore, an abundant research on the corrosion mechanism of LDS should be carried out in the future, aiming to improve the corrosion resistance of LDS by adjusting the alloy element design without affecting the obtained mechanical properties.

**Acknowledgements** This work was financially supported by the National Science and Technology Resources Investigation Program of China (Grant No. 2019FY101400) and the National Natural Science Foundation of China (Nos. 52104319 and 51871024).

## Declarations

**Conflict of interest** The authors state that there are no conflicts of interest to disclose.

## References

- [1] H. Kim, D.W. Suh, N.J. Kim, *Sci. Technol. Adv. Mater.* **14**, 014205 (2013)
- [2] S.H. Kim, H. Kim, N.J. Kim, *Nature* **518**, 77 (2015)
- [3] J.W. Morris, *Nat. Mater.* **16**, 787 (2017)
- [4] O.A. Zambrano, *J. Mater. Sci.* **53**, 14003 (2018)
- [5] J.H. Hwang, T.T.T. Trang, O. Lee, G. Park, A. Zargarán, N.J. Kim, *Acta Mater.* **191**, 1 (2020)
- [6] J. Charles, A. Berghezan, *Cryogenics* **21**, 278 (1981)
- [7] M. Cavallin, F. Felli, R. Frates, F. Veniali, *Werkst. Korros.* **33**, 281 (1982)
- [8] J.C. Benz, H.W. Leavenworth, *JOM* **37**, 36 (1985)
- [9] S.C. Tjong, *Surf. Coat. Technol.* **28**, 181 (1986)
- [10] S.T. Shih, I.F. Tsu, T.P. Perng, *Metall. Trans. A* **24**, 459 (1993)
- [11] M. Ruščák, T.P. Perng, *Corrosion* **51**, 738 (1995)
- [12] S.C. Chang, J.Y. Liu, H.K. Juang, *Corrosion* **51**, 399 (1995)
- [13] Y.S. Zhang, X.M. Zhu, *Corros. Sci.* **41**, 1817 (1999)
- [14] G. Frommeyer, E.J. Drewes, *B. Engl. Rev. Met. Paris* **97**, 1245 (2000)
- [15] M. Koyama, E. Akiyama, K. Tsuzaki, *ISIJ Int.* **53**, 1268 (2013)
- [16] M.C. Ha, J.M. Koo, J.K. Lee, S.W. Hwang, K.T. Park, *Mater. Sci. Eng. A* **586**, 276 (2013)
- [17] A. Rahnama, H. Kotadia, S. Sridhar, *Acta Mater.* **132**, 627 (2017)
- [18] Z. Wang, W. Lu, H. Zhao, C.H. Liebscher, J. He, D. Ponge, D. Raabe, Z. Li, *Sci. Adv.* **6**, 9543 (2020)
- [19] I. Gutierrez-Urrutia, D. Raabe, *Acta Mater.* **60**, 5791 (2012)
- [20] S.M. Allen, J.W. Cahn, *Acta Metall.* **24**, 425 (1976)
- [21] I.I. Gutierrez-Urrutia, D. Raabe, *Scr. Mater.* **68**, 343 (2013)
- [22] M.J. Yao, P. Dey, J.B. Seol, P. Choi, M. Herbig, R.K.W. Marceau, T. Hickel, J. Neugebauer, D. Raabe, *Acta Mater.* **106**, 229 (2016)
- [23] M. Kapoor, D. Isheim, G. Ghosh, S. Vaynman, M.E. Fine, Y.W. Chung, *Acta Mater.* **73**, 56 (2014)
- [24] S.P. Chen, R. Rana, A. Haldar, R.K. Ray, *Prog. Mater. Sci.* **89**, 345 (2017)
- [25] R. Rana, C. Liu, R.K. Ray, *Scr. Mater.* **68**, 354 (2013)
- [26] V.V. Satya Prasad, S. Khaple, R.G. Baligidad, *JOM* **66**, 1785 (2014)
- [27] S. Pramanik, S. Suwas, *JOM* **66**, 1868 (2014)
- [28] A. Zargarán, H.S. Kim, J.H. Kwak, N.J. Kim, *Scr. Mater.* **89**, 37 (2014)
- [29] R.G. Baligidad, *Mater. Sci. Eng. A* **368**, 131 (2004)
- [30] P.C. Chen, C.G. Chao, T.F. Liu, *Scr. Mater.* **68**, 380 (2013)
- [31] C.H. Liebscher, M.J. Yao, P. Dey, M. Lipińska-Chwalek, B. Berkels, B. Gault, T. Hickel, M. Herbig, J. Mayer, J. Neugebauer, D. Raabe, G. Dehm, C. Scheu, *Phys. Rev. Mater.* **2**, 023804 (2018)
- [32] H. Song, Y. Kwon, S.S. Sohn, M. Koo, N.J. Kim, B.J. Lee, S. Lee, *Mater. Sci. Eng. A* **730**, 177 (2018)
- [33] J.X. Liu, H.B. Wua, S.W. Yang, X.P. Yu, C. Ding, *Mater. Lett.* **285**, 811 (2021)
- [34] K.M. Chang, C.G. Chao, T.F. Liu, *Scr. Mater.* **63**, 162 (2010)
- [35] K. Choi, C.H. Seo, H. Lee, S.K. Kim, J.H. Kwak, K.G. Chin, K.T. Park, N.J. Kim, *Scr. Mater.* **63**, 1028 (2010)
- [36] M.X. Yang, F.P. Yuan, Q.G. Xie, Y.D. Wang, E. Ma, X.L. Wu, *Acta Mater.* **109**, 213 (2016)
- [37] S. Jeong, G. Park, B. Kim, J. Moon, S.J. Park, C. Lee, *Mater. Sci. Eng. A* **742**, 61 (2019)
- [38] C.L. Lin, C.G. Chao, J.Y. Juang, J.M. Yang, T.F. Liu, *J. Alloys Compd.* **586**, 616 (2014)
- [39] Z.Q. Wu, H. Ding, X.H. An, D. Ha, X.Z. Liao, *Mater. Sci. Eng. A* **639**, 187 (2015)
- [40] Y. Sutou, N. Kamiya, R. Umino, I. Ohnuma, K. Ishida, *ISIJ Int.* **50**, 893 (2010)
- [41] G. Park, C.H. Nam, A. Zargarán, N.J. Kim, *Scr. Mater.* **165**, 68 (2019)
- [42] S.W. Hwang, J.H. Ji, E.G. Lee, K.T. Park, *Mater. Sci. Eng. A* **528**, 5196 (2011)
- [43] J. Zhang, D. Raabe, C.C. Tasan, *Acta Mater.* **141**, 374 (2017)
- [44] L.X. Xu, H.B. Wu, *Mater. Sci. Eng. A* **738**, 163 (2018)
- [45] S.S. Sohn, H. Song, B.C. Suh, J.H. Kwak, B.J. Lee, N.J. Kim, S. Lee, *Acta Mater.* **96**, 301 (2015)
- [46] W.C. Cheng, Y.S. Song, Y.S. Lin, K.F. Chen, P.C. Pistorius, *Metall. Mater. Trans. A* **45**, 1199 (2013)
- [47] W.J. Lu, X.F. Zhang, R.S. Qin, *Mater. Lett.* **138**, 96 (2015)
- [48] W.C. Cheng, C.Y. Cheng, C.W. Hsu, D.E. Laughlin, *Mater. Sci. Eng. A* **642**, 128 (2015)
- [49] C.L. Lin, C.G. Chao, H.Y. Bor, T.F. Liu, *Mater. Trans.* **51**, 1084 (2010)
- [50] W.C. Cheng, *JOM* **66**, 1809 (2014)
- [51] J.B. Seol, D. Raabe, P. Choi, H.S. Park, J.H. Kwak, C.G. Park, *Scr. Mater.* **68**, 348 (2013)
- [52] L. Bartlett, D.V. Aken, *JOM* **66**, 1770 (2014)
- [53] H. Kim, *Scr. Mater.* **160**, 29 (2019)
- [54] X.X. Xu, H.L. Cheng, W. Wu, Z.Y. Liu, X.G. Li, *Corros. Sci.* **191**, 109760 (2021)
- [55] C.H. Seo, K.H. Kwon, K. Choi, K.H. Kim, J.H. Kwak, S. Lee, N.J. Kim, *Scr. Mater.* **66**, 519 (2012)
- [56] C.J. Wang, Y.C. Chang, *Mater. Chem. Phys.* **76**, 151 (2002)
- [57] Y.S. Li, M. Spiegel, *Oxid. Met.* **61**, 303 (2004)
- [58] Z.G. Zhang, F. Gesmundo, P.Y. Hou, Y. Niu, *Corros. Sci.* **48**, 741 (2006)
- [59] W. Penga, J.J. Wang, H.W. Zhang, X.Y. Hong, Z.Y. Wu, Y.L. Xu, J. Li, X.S. Xiao, *Corros. Sci.* **126**, 197 (2017)
- [60] Y.S. Zhang, X.M. Zhu, S.H. Zhong, *Corros. Sci.* **46**, 853 (2004)
- [61] A.S. Hamada, L.P. Karjalainen, M.A. El-Zeky, *Passivation of metals and semiconductors properties of thin oxide layers* (Elsevier, 2006)
- [62] J. Bosch, U. Martin, W. Aperador, J.M. Bastidas, J. Röss, D.M. Bastidas, *Materials* **14**, 51 (2021)
- [63] X.M. Zhu, Y.S. Zhang, *Corros. Sci.* **54**, 3 (1998)
- [64] Y.S. Zhang, X.M. Zhu, M. Liu, R.X. Che, *Appl. Surf. Sci.* **222**, 89 (2004)
- [65] J. Moon, H.Y. Ha, S.J. Park, T.H. Lee, J.H. Jang, C.H. Lee, H.N. Han, H.U. Hong, *J. Alloys Compd.* **775**, 1136 (2019)
- [66] M.F. Montemor, A.M.P. Simões, M.G.S. Ferreira, M.D.C. Belo, *Corros. Sci.* **41**, 17 (1999)
- [67] G.O. Ilevbare, G.T. Burstein, *Corros. Sci.* **45**, 1545 (2003)
- [68] S. Fajardo, I. Llorente, J.A. Jiménez, J.M. Bastidas, D.M. Bastidas, *Corros. Sci.* **154**, 246 (2019)
- [69] V.F.C. Lins, M.A. Freitas, E.M.P. Silva, *Appl. Surf. Sci.* **250**, 124 (2005)
- [70] Y.H. Tuan, C.S. Wang, C.Y. Tsai, C.G. Chao, T.F. Liu, *Mater. Chem. Phys.* **114**, 595 (2009)
- [71] U. Martin, J. Röss, J. Bosch, D.M. Bastidas, *Appl. Sci.* **10**, 9104 (2020)
- [72] S. Fajardo, I. Llorente, J.A. Jiménez, N. Calderón, D. Herrán-Medina, J.M. Bastidas, J. Röss, D.M. Bastidas, *Appl. Surf. Sci.* **513**, 36 (2020)
- [73] G.D. Tsay, C.L. Lin, C.G. Chao, T.F. Liu, *Mater. Trans.* **51**, 2318 (2010)
- [74] X.Y. Yuan, Y. Zhao, X. Li, L.Q. Chen, *J. Mater. Sci. Technol.* **33**, 1555 (2017)

- [75] Y. Al, M.D. Ilyushechkin, K.G. Dolan, S.D. McLennan, Sharma. *Asia-Pac. J. Chem. Eng.* **7**, 716 (2012)
- [76] D. Raabe, H. Springer, I. Gutierrez-Urrutia, F. Roters, M. Bausch, J.B. Seol, M. Koyama, P.P. Choi, K. Tsuzaki, *JOM* **66**, 1845 (2014)
- [77] T.A. Timmerscheidt, P. Dey, D. Bogdanovski, J.V. Appen, T. Hickel, J. Neugebauer, R. Dronskowski, *Metals* **7**, 43 (2017)
- [78] S.C. Tjong, C.S. Wu, *Mater. Sci. Eng. A* **80**, 203 (1986)
- [79] S.C. Tjong, *Werkst. Korros.* **37**, 444 (1986)
- [80] S.C. Tjong, *J. Mater. Sci.* **21**, 1166 (1986)
- [81] K.H. So, J.S. Kim, Y.S. Chun, K.T. Park, Y.K. Lee, C.S. Lee, *ISIJ Int.* **49**, 1952 (2009)
- [82] D.K. Han, Y.M. Kim, H.N. Han, H.K.D.H. Bhadeshia, D.W. Suh, *Scr. Mater.* **80**, 9 (2014)
- [83] T. Dieudonné, L. Marchetti, M. Wery, F. Miserque, M. Tabarant, J. Chêne, C. Allely, P. Cugy, C.P. Scott, *Corros. Sci.* **83**, 234 (2014)
- [84] I.J. Park, K.H. Jeong, J.G. Jung, C.S. Lee, Y.K. Lee, *Int. J. Hydrogen Energy* **37**, 9925 (2012)
- [85] M. Koyama, H. Springer, S.V. Merzlikin, K. Tsuzaki, E. Akiyama, D. Raabe, *Int. J. Hydrogen Energy* **39**, 4634 (2014)
- [86] E.J. Song, H.K.D.H. Bhadeshia, D.W. Suh, *Scr. Mater.* **87**, 9 (2014)
- [87] D.K. Han, S.K. Lee, S.J. Noh, S.K. Kim, D.W. Suh, *Scr. Mater.* **99**, 45 (2015)